Acta Biomaterialia 23 (2015) 347–353

Contents lists available at ScienceDirect

Acta Biomaterialia

journal homepage: www.elsevier.com/locate/actabiomat

Influence of trace impurities on the *in vitro* and *in vivo* degradation of biodegradable Mg–5Zn–0.3Ca alloys

J. Hofstetter [a], E. Martinelli [b], S. Pogatscher [a], P. Schmutz [c], E. Povoden-Karadeniz [d], A.M. Weinberg [b], P.J. Uggowitzer [a], J.F. Löffler [a,*]

[a] Laboratory of Metal Physics and Technology, Department of Materials, ETH Zurich, 8093 Zurich, Switzerland
[b] Department of Orthopaedics and Orthopaedic Surgery, Medical University Graz, 8036 Graz, Austria
[c] Laboratory for Joining Technologies and Corrosion, EMPA, Swiss Federal Laboratories for Materials Science and Technology, 8600 Dübendorf, Switzerland
[d] Christian Doppler Laboratory for Early Stages of Precipitation, Vienna University of Technology, 1040 Vienna, Austria

ARTICLE INFO

Article history:
Received 31 January 2015
Received in revised form 5 May 2015
Accepted 9 May 2015
Available online 15 May 2015

Keywords:
Magnesium
Mg–Zn–Ca alloys
Biodegradation
Intermetallic phases
Corrosion

ABSTRACT

The hydrogen evolution method and animal experiments were deployed to investigate the effect of trace impurity elements on the degradation behavior of high-strength Mg alloys of type ZX50 (Mg–5Zn–0.3Ca). It is shown that trace impurity elements increase the degradation rate, predominantly in the initial period of the tests, and also increase the material's susceptibility to localized corrosion attack. These effects are explained on the basis of the corrosion potential of the intermetallic phases present in the alloys. The Zn-rich phases present in ZX50 are nobler than the Mg matrix, and thus act as cathodic sites. The impurity elements Fe and Mn in the alloy of conventional purity are incorporated in these Zn-rich intermetallic phases and therefore increase their cathodic efficiency. A design rule for circumventing the formation of noble intermetallic particles and thus avoiding galvanically accelerated dissolution of the Mg matrix is proposed.

1. Introduction

Magnesium alloys are of special interest in the context of structural lightweight applications in the transport and aerospace industries, and for temporary implants in medicine because of their biocompatibility and biodegradability [1,2]. One of the major obstacles to widespread application of magnesium alloys, however, is their high corrosion rate [3,4], which is often attributed to the presence of specific impurity elements. Elements such as Fe, Ni, Cu and Co can significantly accelerate Mg corrosion when their concentrations are above their tolerance limits [5–9]. Fe, for example, is the most common impurity element; its tolerance limit is reported as 170 ppm in unalloyed as-cast Mg [3] and roughly 5 ppm in wrought Mg [6,9]. Below this limit, when no Fe-rich particles are formed and thus no electrochemically active cathodic sites exist to accelerate corrosive attack, the corrosion rate decreases dramatically. Recent studies have added silicon (Si) to the above-mentioned reactive impurity elements detrimental to corrosion. Si plays a critical role in promoting the formation and growth of Fe-rich particles and should thus also be considered as corrosion-provoking element [9,10].

For osteosynthesis implants and stent applications, not only electrochemical and biocompatible requirements are crucial, but also mechanical properties [1]. Recent studies have demonstrated that the alloying system Mg–Zn–Ca offers simultaneous high strength and high ductility, with values of $R_{p0.2} > 250$ MPa, $R_m > 300$ MPa and $A_f > 20\%$. These attractive large values were achieved within a composition window of 5–6 wt.% Zn and 0.2–0.4 wt.% Ca [11,12]. Recently the *in vivo* behavior of an alloy with 5 wt.% Zn and 0.25 wt.% Ca (ZX50) of conventional purity (CP) was investigated, and undesired rapid degradation was observed [13]. In the present study, the alloy ZX50 was chosen again, but this time raw materials of two different purities were used. The first alloy was made of CP Mg identical to that used in [13], but the second was synthesized using ultrahigh-purity (XHP) Mg [14]. The research aim of this study was to compare the *in vitro* and *in vivo* behavior of the two alloys CP ZX50 and XHP ZX50, and to clarify the influence of trace elements on degradation characteristics and mechanisms. The *in vitro* corrosion was determined via the hydrogen evolution method [15], deploying a newly designed testing device [9]. For the *in vivo* examination pins of each alloy were implanted in the femoral shafts of rats and their degradation was studied over a period of 12 weeks (see also Ref. [13]). A few pins were also explanted after two weeks to investigate their surface topography and elucidate the degradation mechanisms.

* Corresponding author. Tel.: +41 44 632 2565; fax: +41 44 633 1421.
E-mail address: joerg.loeffler@mat.ethz.ch (J.F. Löffler).

http://dx.doi.org/10.1016/j.actbio.2015.05.004
1742-7061/

2. Experimental methods

2.1. Materials and methods

CP and XHP ZX50 were each processed to extruded rods, from which specimens for the *in vivo* and *in vitro* tests were machined. Conventional pure Mg (99.95%), Zn (99.5%), and Ca (99.5%) were used as raw materials for CP ZX50. Mg and the alloying elements were melted in an electric furnace at a temperature of approximately 690 °C, treated with $MnCl_2$ to reduce the Fe-content [16], and then cast by vertical direct chill casting on an industrial scale (billet diameter: 185 mm) at a speed of approximately 1.6 mm/s with continuous water cooling. The alloy XHP ZX50 was produced using XHP Mg (99.999%), Zn (99.999%), and Ca (99.99%). The ultrahigh-purity (XHP) Mg was produced using an in-house vacuum distillation setup to reduce the impurity content of conventional-pure (CP) Mg. High-purity graphite crucibles were used to avoid any contamination [9,14]. The raw materials of XHP ZX50 were synthesized using a protective gas mixture (pure Ar with 1 vol.% of SF_6) at 750 °C. The melt was poured into a graphite crucible of approx. 150 mm in height and 55 mm in diameter. Directional solidification was achieved by cooling the bottom of the mold, which ensures cavity-free shrinkage. The CP and XHP ZX50 cast billets were both homogenized at 330 °C for 12 h, cooled with pressurized air and machined to extrusion billets. The sizes of the extrusion billets were 120 mm in diameter and 250 mm in length for CP ZX50, and 50 mm in diameter and 120 mm in length for XHP ZX50. Direct extrusion was performed at 325 °C with a ram speed of ≈0.5 mm/s for both alloys. The extruded rods had diameters of 20 mm for CP ZX50 and 8 mm for XHP ZX50, which corresponds to extrusion ratios of 36:1 and 39:1, respectively. Table 1 shows the chemical compositions of the alloys, determined by glow discharge mass spectrometry in the as-cast state.

Samples for *in vitro* tests were prepared from the extruded rods; the sample surfaces were 857 ± 2.8 mm^2 for CP ZX50 and 459 ± 12.8 mm^2 for XHP ZX50. These surface areas result from the different rod diameters used to ensure similar extrusion ratios. Pins for the *in vivo* tests were machined to 1.6 mm in diameter and 8 mm in length, corresponding to a total surface area of approx. 44 mm^2 and an initial volume of ~16 mm^3. The *in vitro* samples were ground using abrasive SiC paper of granularity 4000 and then polished with a 1 μm polishing cloth. The samples were cleaned in an ultrasonic bath using isopropyl alcohol and dried in hot air just before immersion. The specimens for the *in vivo* tests were cleaned in a cascade of pure ethanol in an ultrasonic bath and dried with hot air.

The microstructure analysis of the as-extruded material was performed by optical microscopy (OM) after etching with picric acid. The average grain size was determined using the linear intercept method. Elemental distribution maps of alloy microstructure and the surfaces of explanted pins were recorded using a Hitachi SU-70 scanning electron microscope (SEM, Schottky-type field emission gun), equipped with an X-Max energy dispersive X-ray (EDX) detector from Oxford instruments. The SEM was operated at 15 kV in the secondary electron (SE) and back-scattered electron (BSE) imaging modes. For SEM investigations, the pins were embedded longitudinally in Bakelite with some bony material at their surfaces. The embedded samples were coated with an 8-nm-thick carbon layer using a Balzers SCD 050 sputter coater.

2.2. In vitro testing

The *in vitro* degradation of each alloy was analyzed using the hydrogen evolution method [15]. Three samples per batch were tested in CO_2-buffered simulated body fluid (SBF) [17] over two weeks of immersion. The immersion tests were performed using a special setup, designed in-house, for slow-corroding material and investigated under the conditions given in Ref. [9]. This setup has the advantages of very stable pH and temperature control, and the possibility to correct for atmospheric pressure fluctuations and gas dissolution [9]. It has already been shown to adequately simulate the *in vivo* situation of pure Mg, Y-containing Mg alloys, and other Mg–Zn–Ca alloying systems [9,18,19]. The pH was set to 7.44 ± 0.043 with a temperature of 36.8 ± 0.34 °C, and the atmospheric pressure was 1008.72 ± 6.86 mbar during the two weeks of immersion. All data points were corrected for pressure fluctuations and gas dissolution, and the mean hydrogen amount was evaluated to ml/cm^2 [9].

2.3. In vivo testing

The animal experiments were conducted according to established principles of ethical respect for animals, and authorized by the Austrian Ministry of Science and Research (BMWF-66.010/0087-II/3b/2011). Eight male Sprague–Dawley® rats with body weights of 140–160 g and 5 weeks of age were used. Under general anesthesia each rat had two identical pins implanted in its femur shafts. An accurate description of the surgical procedure and postoperative treatment is given in Ref. [13]. Micro-computer tomography (μCT) scans were performed at four prearranged times after pin implantation: 1 week, 4 weeks, 8 weeks and 12 weeks. During the μCT examinations the animals were anesthetized using volatile isoflurane (Forane®, Abbot AG, Baar, Switzerland). The rats were scanned using a Siemens Inveon Acquisition Workplace (version 1.2.2.2). Scans were performed at 70 kV voltage, 500 μA current, and with 1000 ms exposure time. The volume of each implant was measured by 3-D morphometric analysis and quantified using the software program 'Mimics®' (Version 15.0, Materialise, Leuven, Belgium); for more details see Ref. [13]. Two rats were euthanized after 2 weeks to inspect the surface topography and elemental distribution in the near-surface regions of the pins. Note that for the present study only the alloy XHP ZX50 was used for the *in vivo* testing. μCT data and explanted pins for surface topography investigations of the alloy CP ZX50 were taken from Kraus et al. [13]. Both the CP ZX50 [13] and XHP ZX50 studies were conducted according to Standard Operation Protocols (SOPs), which were established in the same working group using the same infrastructure, software and animal model. They are thus comparable.

3. Results

3.1. Microstructure

Fig. 1 shows the microstructure of the alloys tested. The grain size D of CP ZX50 is slightly smaller ($D \approx 6$ μm) than that of XHP ZX50 ($D \approx 7.5$ μm). Both alloys contain second-phase particles,

Table 1
Chemical compositions of CP ZX50 (conventional purity) and XHP ZX50 (ultrahigh-purity), where ppm relates to parts per million by weight.

Alloy	Zn (wt.%)	Ca (wt.%)	Mn (ppm)	Si (ppm)	Fe (ppm)	Cu (ppm)	Ni (ppm)	Co (ppm)
CP ZX50	5.24	0.27	1630	440	42	9	8	8
XHP ZX50	5.26	0.31	0.8	2.9	0.5	0.09	0.05	<0.05

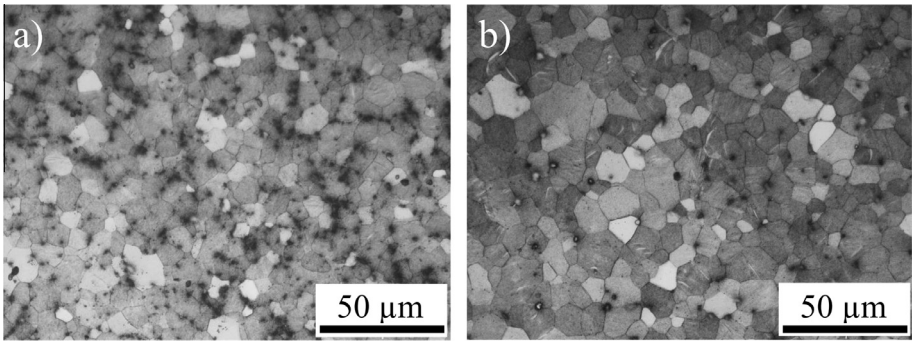

Fig. 1. Optical microscopy images of the microstructures of (a) CP ZX50 and (b) XHP ZX50, extruded at 325 °C.

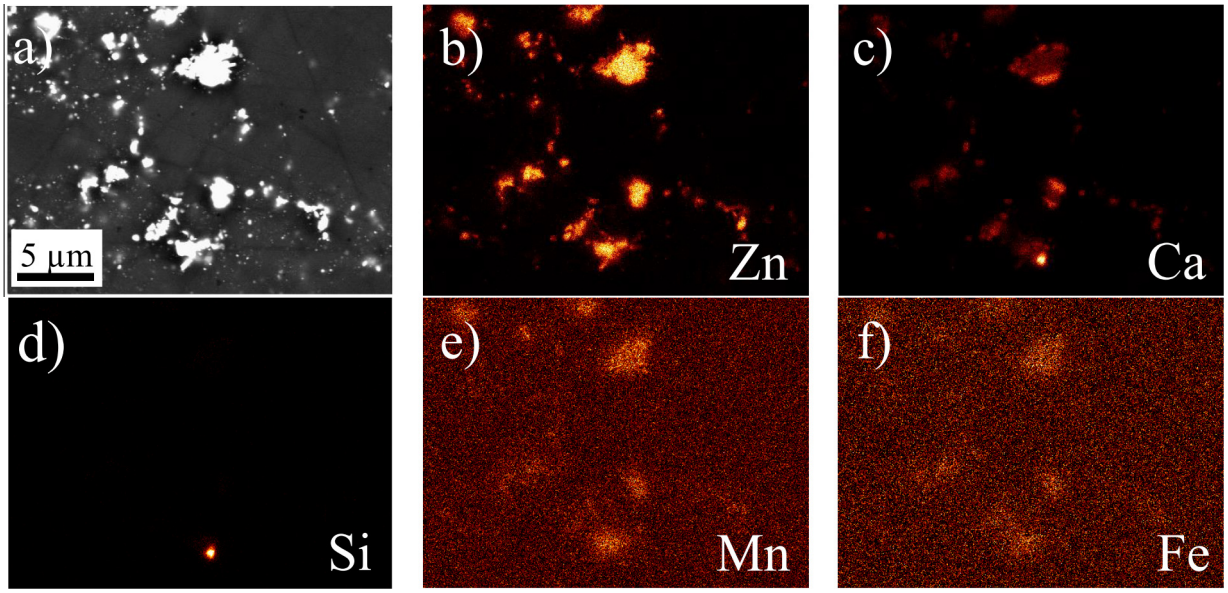

Fig. 2. SEM/EDX images of the microstructure of CP ZX50 extruded at 325 °C.

examples of which are shown in SEM images of CP ZX50 in Fig. 2. These intermetallic particles (IMPs) contain Zn and Ca, and in the case of CP ZX50 also Fe and Mn. Si- and Ca-containing IMPs were also detected very sporadically in CP ZX50. In XHP ZX50, however, only Zn and Ca were found to be present in the IMPs (not shown here). Because the grain size in both alloys is similar, the potential effect of grain size on corrosion rate can be disregarded, in contrast to the effects of impurities and IMPs.

3.2. In vitro immersion testing

The degradation rates of CP and XHP ZX50 characterized by hydrogen evolution revealed clear differences between the alloys. Fig. 3a shows the mean hydrogen evolution as a function of immersion time for both alloys. Conventional-pure CP ZX50 clearly degrades faster than XHP ZX50, monitored by the fact that the former releases much more hydrogen than its counterpart XHP ZX50 after an initiation time of 4 days. The alloy CP ZX50, depicted in the upper insert to Fig. 3a, exhibits strongly inhomogeneous degradation. This inhomogeneity is also illustrated in the optical microscopy cross-section image in Fig. 3b, which demonstrates the corrosion attack at the surface of the sample. The alloy XHP ZX50 shows much more homogeneous degradation behavior (at least during the test period of 16 days), as illustrated in the lower insert of Fig. 3a and the cross-section image of Fig. 3c.

3.3. Animal studies

Fig. 4 illustrates the *in vivo* degradation performance of CP and XHP ZX50 after 1, 4, 8 and 12 weeks of implantation in the rat's femoral shaft. Fig. 4a displays the volume loss as a function of implantation time. The standard deviations in this plot are relatively high. This is the consequence of using different animals with different feeding behaviors and movement activity, and thus different weights and growth [20]. This has an effect on metabolism, healing processes, and blood flow, and thus also on implant degradation. All pins had an initial volume V_0 of approx. 16 mm^3 and their volumes decreased within the study period. After 1 week, the volume loss was 6.6% for CP and 3.4% for XHP ZX50, i.e. during the first period CP ZX50 degraded significantly faster than XHP ZX50. With prolonged degradation time, the difference in absolute volume loss between CP and XHP ZX50 increased monotonically until week 8, but then decreased between weeks 8 and 12. Related to the actual pin volume, however, the volume loss rate was always higher for CP than for XHP ZX50: between weeks 1 and 4, it is calculated to be 8.8%/week for CP and 5.3%/week for XHP ZX50; between weeks 4 and 8 it is 15.8%/week for CP and 9.5%/week for XHP ZX50; and between weeks 8 and 12 it is 17.3%/week for CP and 16.0%/week for XHP ZX50. These numbers illustrate that the difference in degradation rate caused by the difference in purity is high at the beginning and diminishes with

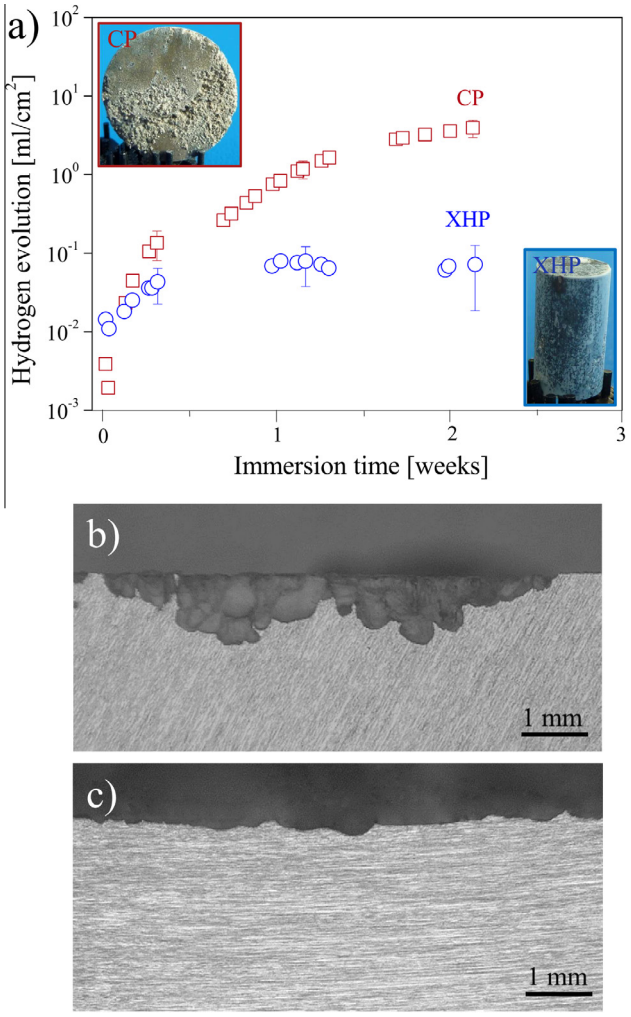

Fig. 3. (a) Mean hydrogen evolution as a function of immersion time for the alloys CP and XHP ZX50 immersed in CO_2-buffered SBF at 37 °C. The upper insert shows CP ZX50 after 380 h of immersion in SBF. The lower insert depicts XHP ZX50 after the same immersion time. Three error bars per alloy are included to demonstrate the data scatter. (b, c) Optical microscope cross-sections illustrating the corrosion attack at the surface of (b) CP ZX50 and (c) XHP ZX50 after two weeks of immersion.

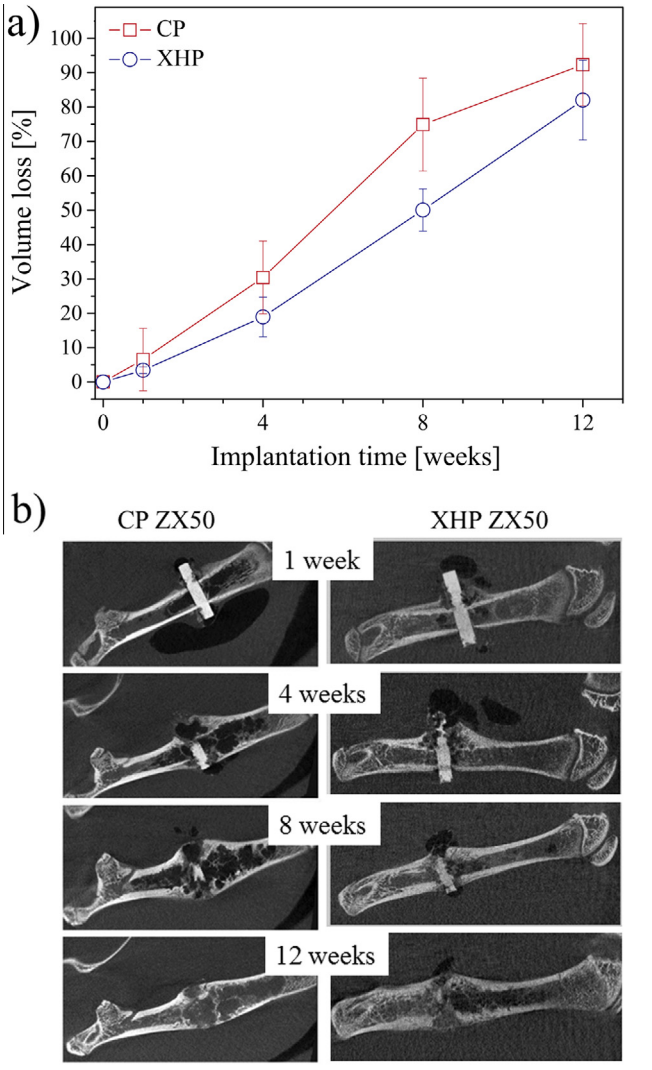

Fig. 4. (a) Pin volume loss for CP ZX50 and XHP ZX50 after 1, 4, 8 and 12 weeks of implantation in the femoral shaft of Sprague–Dawley rats. (b) μCT reconstructions (two-dimensional slices) of CP and XHP ZX50 from four different time periods (1, 4, 8, 12 weeks). CP ZX50 has a higher degradation rate in the first period following implantation; however, nearly complete degradation was observed in both cases after 12 weeks. μCT reconstructions for CP ZX50 were taken from [13].

increasing degradation time. Thus, localized degradation is more pronounced for CP ZX50 than for XHP ZX50 during the first period after implantation, as also observed in the *in vitro* studies. With increasing test duration, however, both alloys exhibit considerable local corrosion attack, and sections of the pins suffering from pronounced localized corrosion degrade faster than other regions dissolving uniformly (see Fig. 4b).

4. Discussion

The results of the investigation reveal clearly the influence of the trace impurity level (see Table 1) on the degradation rate of ZX50 alloys. The alloy made with XHP Mg degrades more slowly *in vitro* and *in vivo* than the alloy with an increased impurity level, but primarily during the first period after implantation. The degradation difference between CP and XHP ZX50 is most significant in the first period of immersion, as can be observed from the optical microscopy cross-sections of the *in vitro* samples in Fig. 3. With increasing test duration, the difference in degradation rate between CP and XHP ZX50 becomes less pronounced, as demonstrated by the *in vivo* results shown in Fig. 4a. Interestingly, despite its high purity, XHP ZX50 also exhibits a high degradation rate relative to Mg–Zn–Ca alloys with low Zn content [19] or unalloyed Mg [9]. These observations are discussed in detail below. A hypothesis for the steady *in vitro* degradation of XHP ZX50 at the end of the immersion test (Fig. 3a) is also presented, explaining the more severe localized corrosion of the *in vivo* pins compared to the *in vitro* samples after two weeks.

Fig. 5 depicts the constitution of the alloy CP ZX50, calculated using MatCalc simulation software with database mc_mg_v1.009 [21]. Two types of intermetallic particles, IM1 and IM3, are present at the extrusion temperature (325 °C) [22]. Their chemical compositions at 325 °C are calculated for IM1 as 53% Zn, 30.5% Mg, and 16.5% Ca, and for IM3 as 77% Zn, 15% Mg, and 8% Ca (in wt.%), i.e. both IMPs contain a high Zn content. The MatCalc Mg database does not list Fe, and thus the impact of the trace elements Fe, Mn and Si on the microstructure was simulated using the Pandat software package with the PanMg2013 database [23]. The presence of 0.12 mol-% CaMgSi and 0.028 mol-% bcc (92% Mn, 7% Fe, 0.5% Si, and 0.5% Zn; in wt.%) phases was predicted at 325 °C.

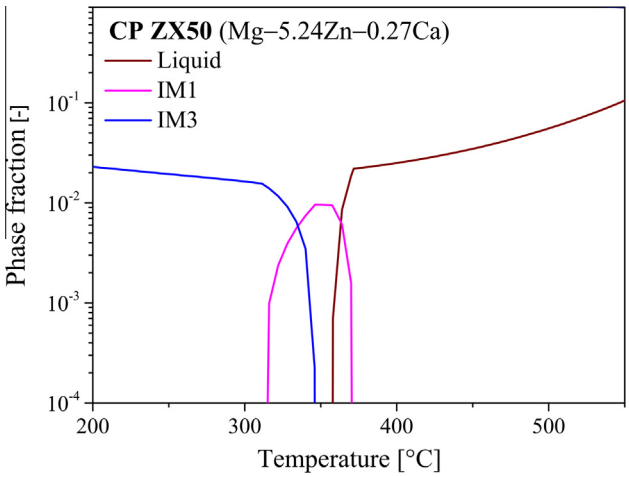

Fig. 5. Constitution of alloy CP ZX50 with 5.24 wt.% Zn and 0.27 wt.% Ca. The intermetallic phases IM1 and IM3 are present at the processing (extrusion) temperature of 325 °C.

The formation of two IMPs with different Zn and Ca contents (IM1: $Ca_3Mg_xZn_{15-x}$, $4.6 \leqslant x \leqslant 12$; IM3: $Ca_2Mg_5Zn_{13}$ (in at.%) [24,25]) is confirmed by the SEM/EDX analysis shown in Fig. 2. They appear to be interconnected with a sharp gradient between sections of high and low Ca content (Fig. 2c). This situation can be explained by the fact that IM1 is formed from the melt and is subsequently partially transformed to IM3 upon annealing and extrusion at 325 °C. Besides the phases IM1 and IM3, the predicted formation of CaMgSi particles is also confirmed in Fig. 2c and d. Interestingly and contrary to expectations, Mn and Fe are incorporated into the Zn–Mg–Ca particles. Whereas it is not completely clear whether Mn and Fe are in solid solution or present as very fine bcc phase combined with IM1/IM3, it is evident that they do not form separate isolated phases. Irrespective of whether Mn and Fe are in solid solution or incorporated as fine IMPs, however, it can be assumed that their presence changes the electrochemical properties of the Zn-rich IM1 and IM3 phases in the direction of higher electrochemical potential and possibly higher cathodic hydrogen reduction rates. Thus, the IMPs in CP ZX50 are expected to be nobler and more reactive than their counterparts in XHP ZX50.

Regardless of their trace element content, Mg–Zn–Ca alloys with high Zn content are still prone to corrosion attack in physiological environments. It is generally agreed that the formation of ternary intermetallic phases with high Zn content is the main reason for increased degradation susceptibility [26–30]. Because of their higher (nobler) corrosion potential compared to the Mg matrix when both phases are considered separately, the IMPs induce galvanic coupling interactions, with locally enhanced anodic dissolution of the material's matrix. Such corrosion attack is shown for example in Fig. 6, which illustrates the near-surface morphology of an XHP ZX50 pin explanted after 2 weeks in a rat's femoral shaft. The degradation attack is characterized by the local formation of pits, with accelerated Mg matrix dissolution resulting from the presence of the cathodic Zn-rich IMPs. Propagation of local attack via pit formation leads in turn to a pronounced acceleration of the degradation rate. This 'autocatalytic' process is well understood for materials such as stainless steel and aluminum which present good cation hydrolysis properties [31], but no generally accepted description exists so far for materials with Mg cations that are difficult to hydrolyze. Nevertheless, several arguments are given in the literature which can provide a convincing explanation [32–34]. They are all based on the description of chemical processes that occur inside surface pits, i.e. the formation of the previously mentioned autocatalytic corrosion mechanism which generates a pronounced localized corrosion breakdown. However, Mg in contact with aqueous SBF cannot solely explain this acceleration. One more critical reason appears to be the enrichment of 'remaining' cathodically reactive IMPs inside the pits caused by the dissolution of the matrix, as shown in Fig. 6e.

In comparison with the ZX50 alloys, XHP Mg–Zn–Ca alloys with low Zn content exhibit very slow and homogeneous degradation. As an example, the volume loss of an alloy with only 1 wt.% Zn and 0.3 wt.% Ca (XHP ZX10) is roughly 1% after four weeks of implantation [19], whereas the volume loss of XHP ZX50 is ≈20% after the same time period and under otherwise comparable *in vivo* conditions. The CP ZX50 volume loss is then already ≈30% at this stage. This strongly differing degradation behavior is caused

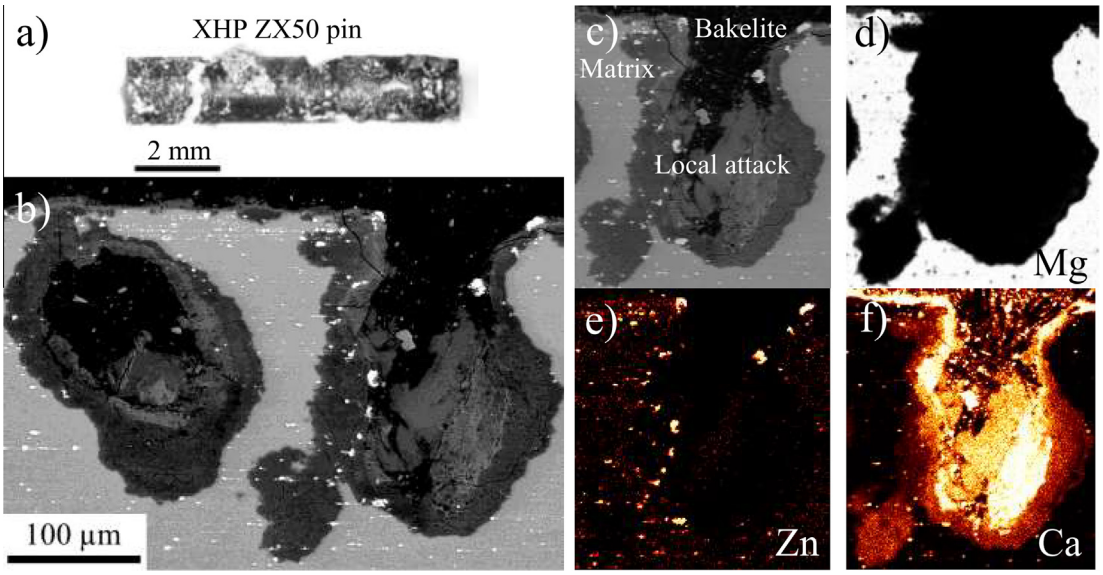

Fig. 6. Explanted XHP ZX50 pin after two weeks of implantation in a femoral shaft of a rat. (a) Optical microscopy image of the entire pin. (b) BSE image of two pits caused by local attack at the bone-implant interface. (c) Close-up of the larger pit with EDX mapping of the elements (d) Mg, (e) Zn and (f) Ca. Zn enrichment takes place in the pits; Ca is deposited from the environment [1] as biological calcium phosphate.

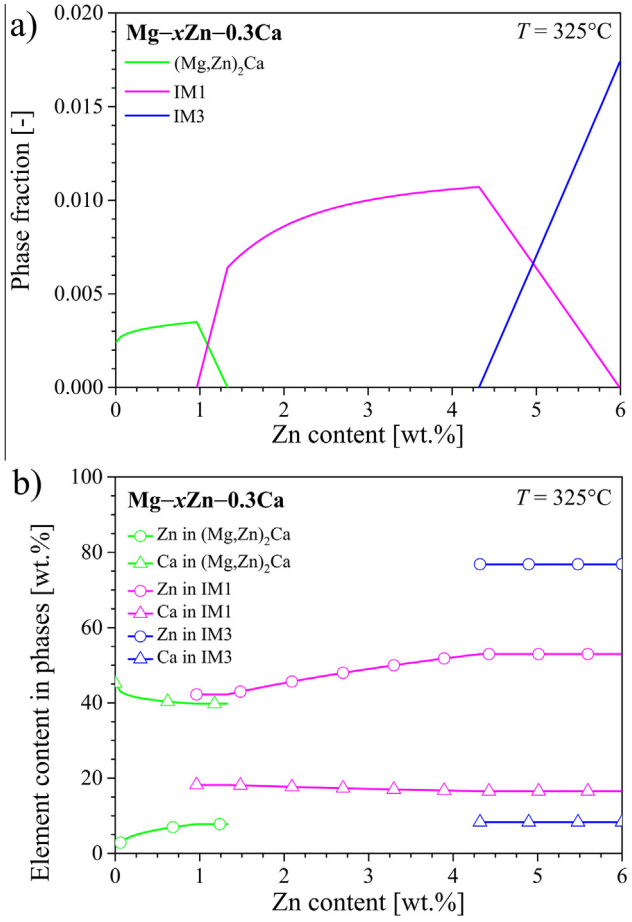

Fig. 7. (a) Phase fraction of IMPs and (b) their chemical compositions in Mg–*x*Zn–0.3Ca at 325 °C in dependence on the Zn content. Calculated using MatCalc simulation software with database mc_mg_v1.009 [21].

by the different electrochemical nature of the intermetallic phases, as illustrated in Fig. 7. At high Zn content, i.e. ≈5 wt.%, IMPs of type IM1 and IM3 are present, whereas at a Zn content ⩽1 wt.% only the Laves phase $(Mg,Zn)_2Ca$ precipitates at $T = 325$ °C. The phases IM1 and IM3 contain large amounts of Zn and are thus of cathodic nature, i.e. they are nobler than the matrix, whereas the phase $(Mg,Zn)_2Ca$ has a high Ca and low Zn content and is therefore less noble than the matrix. This phase now acts as an anodic site, i.e. does not cause accelerated galvanic dissolution of the Mg matrix [19,35,36]. Südholz et al. investigated the electrochemical properties of several Mg-based IMPs and all were found to be cathodic to Mg, with the exception of Mg_2Ca [34]. Based on this work, a detailed electrochemical characterization of the IMPs is planned in a further study. From the above discussion, it becomes clear that Mg–Zn–Ca alloys with low degradation rates should be designed with the provision of avoiding the formation of Zn-rich IMPs, i.e. the Zn content should be kept at or below 1 wt.%.

The higher degradation rate of CP ZX50 compared to XHP ZX50 becomes plausible if one accepts that that (i) noble Zn-rich IMPs accelerate anodic dissolution of the Mg matrix and (ii) trace elements such as those present in CP ZX50 (Fe, Cu, Ni, Co, Si, Mn) additionally increase the cathodic reactivity of these IMPs. The presence of very reactive cathodic impurities in IMPs controls the initial stage of corrosion processes and explains why CP ZX50 corrodes faster than XHP ZX50 as soon as it is exposed to SBF or *in vivo* conditions. The first period of the hydrogen evolution measurement is related to the necessity of first degrading an initially protecting oxy-hydroxide in this buffered solution before efficient cathodic activity can be achieved. The role of the carbonates related to the CO_2 buffering in Mg or Zn hydroxide stabilization is still under investigation and may explain the corrosion rate differences observed in the initial stages of the *in vitro* and *in vivo* experiments.

With increasing test duration the effect of the impurities becomes less pronounced, because the influence of their higher cathodic activity in 'contaminated' IMPs is then masked by the additional effects of local autocatalytic corrosion in the pits formed. In particular, the progressive increase of Zn-rich surface area due to the release of Zn-rich IMPs in the pits (see Fig. 6c) generates additional local cathodic sites. This in turn explains why a lower Zn content (resulting in the absence of IM1 and IM3 IMPs) leads to much lower degradation rate, as reported for the alloy ZX10 in Ref. [19]. In addition, the presence of CaMgSi IMPs may influence the local attack at the beginning of the tests, as they are known to show cathodic corrosion behavior [37].

5. Conclusion

Bioresorbable Mg alloys of type ZX50 (Mg–5Zn–0.3Ca) exhibit rapid and inhomogeneous *in vitro* and *in vivo* degradation. A reduction in the impurity level to very low values decreases the degradation rate, but mostly only during the first period after implantation. The ZX50 alloys are characterized by the presence of Zn-rich IMPs. These IMPs are nobler than the Mg matrix and therefore act as cathodic sites. Local attack and galvanically accelerated dissolution of the matrix cause the formation of pits, which in turn generate autocatalytic corrosion. Impurities such as Fe and Mn are incorporated in the Zn-rich IMPs, generating additional cathodic reactivity. This leads to accelerated localized corrosion of CP ZX50 and thus to a higher degradation rate in CP ZX50 compared to its ultrahigh-purity counterpart. The impurities mainly influence the initial degradation, whereas with progressive time the release of Zn-rich IMPs in the forming pits dominates the corrosion behavior. At this later stage, the degradation rates of CP and XHP ZX50 become similar. Such Zn-rich IMPs do not form in the Zn-lean alloy ZX10, and thus it shows much less degradation than ZX50.

Acknowledgements

The authors gratefully acknowledge financial support by the Swiss National Science Foundation (SNF Grant No. 200021-157058) and by the Laura Bassi Center of Expertise BRIC (Bioresorbable Implants for Children), FFG, Austria.

Appendix A. Figures with essential color discrimination

Certain figures in this article, particularly Figs. 2–7, are difficult to interpret in black and white. The full color images can be found in the on-line version, at doi: http://dx.doi.org/10.1016/j.actbio.2015.05.004.

References

[1] F. Witte, V. Kaese, H. Haferkamp, E. Switzer, A. Meyer-Lindenberg, C.J. Wirth, et al., In vivo corrosion of four magnesium alloys and the associated bone response, Biomaterials 26 (2005) 3557–3563.
[2] Y.F. Zheng, X.N. Gu, F. Witte, Biodegradable metals, Mater. Sci. Eng. 77 (2014) 1–34.
[3] G.L. Song, A. Atrens, Corrosion mechanisms of magnesium alloys, Adv. Eng. Mater. 1 (1999) 11–33.
[4] I.J. Polmear, Light Alloys: Metallurgy of the Light Metals, second ed., Edward Arnold, London, England, 1989.
[5] G. Song, A. Atrens, Understanding magnesium corrosion. A framework for improved alloy performance, Adv. Eng. Mater. 5 (2003) 837–858.
[6] M. Liu, P.J. Uggowitzer, A.V. Nagasekhar, P. Schmutz, M. Easton, G.-L. Song, et al., Calculated phase diagrams and the corrosion of die-cast Mg–Al alloys, Corros. Sci. 51 (2009) 602–619.

[7] G.L. Makar, J. Kruger, Corrosion studies of rapidly solidified magnesium alloy, Electrochem. Soc. 137 (1990) 414–421.
[8] J.D. Hanawalt, C.E. Nelson, J.A. Peloubet, Corrosion studies of magnesium and its alloys, Trans. AIME 147 (1942) 273–298.
[9] J. Hofstetter, E. Martinelli, A.M. Weinberg, M. Becker, B. Mingler, P.J. Uggowitzer, et al., Assessing the degradation performance of ultrahigh-purity magnesium in vitro and in vivo, Corros. Sci. 91 (2015) 29–36.
[10] L. Yang, X. Zhou, S.-M. Liang, R. Schmid-Fetzer, Z. Fan, G. Scamans, et al., Effect of traces of silicon on the formation of Fe-rich particles in pure magnesium and the corrosion susceptibility of magnesium, J. Alloys Compd. 619 (2015) 396–400.
[11] A.C. Hänzi, A.S. Sologubenko, P. Gunde, M. Schinhammer, P.J. Uggowitzer, Design considerations for achieving simultaneously high-strength and highly ductile magnesium alloys, Philos. Mag. Lett. 92 (2012) 417–427.
[12] P. Gunde, A.C. Hänzi, A. Sologubenko, P.J. Uggowitzer, High-strength magnesium alloys for degradable implant applications, Mater. Sci. Eng. A 528 (2011) 1047.
[13] T. Kraus, S.F. Fischerauer, A.C. Hänzi, P.J. Uggowitzer, J.F. Löffler, A.M. Weinberg, Magnesium alloys for temporary implants in osteosynthesis: in vivo studies of their degradation and interaction with bone, Acta Biomater. 8 (2012) 1230–1238.
[14] J.F. Löffler, P.J. Uggowitzer, C. Wegmann, M. Becker, H.K. Feichtinger, Process and apparatus for vacuum distillation of high-purity magnesium. European Patent Application PCT/EP 2013/000131 – WO2013/1076442012.
[15] G. Song, A. Atrens, D.H. StJohn, A hydrogen evolution method for the estimation of the corrosion rate of magnesium alloys, Magnesium Technology Conference at TMS, New Orleans, LA, USA, 2001, pp. 255.
[16] G. Wu, H. Gao, W. Ding, Y. Zhu, Study on mechanism of iron reduction in magnesium alloy melt, J. Mater. Sci. 40 (2005) 6175–6180.
[17] L. Müller, F.A. Müller, Preparation of SBF with different content and its influence on the composition of biomimetic apatites, Acta Biomater. 2 (2006) 181–189.
[18] M. Schinhammer, J. Hofstetter, C. Wegmann, F. Moszner, J.F. Löffler, P.J. Uggowitzer, On the immersion testing of degradable implant materials in simulated body fluid: active pH regulation using CO2, Adv. Eng. Mater. (2013).
[19] J. Hofstetter, M. Becker, E. Martinelli, A.M. Weinberg, B. Mingler, H. Kilian, et al., High-strength low-alloy (HSLA) Mg–Zn–Ca alloys with excellent biodegradation performance, JOM 66 (2014) 566–572.
[20] Janvier Labs, Research Model 'Sprague Dawley', <http://www.janvier-labs.com/tl_files/_media/images/FICHE_RESEARCH_MODEL_SPRAGUE_DAWLEY.pdf>. 2015.
[21] E. Kozeschnik, Current MatCalc version 5.61.057. <http://www.matcalc.tuwien.ac.at/>.
[22] M. Mezbahul-Islam, Y.N. Zhang, C. Shekhar, M. Medraj, Critical assessment and thermodynamic modeling of Mg–Ca–Zn system supported by key experiments, Calphad 46 (2014) 134–147.
[23] Pandat, CompuTherm LLC, Software package for calculating phase diagrams and thermodynamic properties of multi-component alloys, <http://www.computhermcom/>, Madison, WI 53719 USA.
[24] Y.N. Zhang, X.D. Liu, Z. Altounian, M. Medraj, Coherent nanoscale ternary precipitates in crystallized Ca4Mg72Zn24 metallic glass, Scr. Mater. 68 (2013) 647–650.
[25] Y.N. Zhang, D. Kevorkov, F. Bridier, M. Medraj, Experimental study of the Ca–Mg–Zn system using diffusion couples and key alloys, Sci. Technol. Adv. Mater. 12 (2011) 025003.
[26] H.R. Bakhsheshi-Rad, M.R. Abdul-Kadir, M.H. Idris, S. Farahany, Relationship between the corrosion behavior and the thermal characteristics and microstructure of Mg–0.5Ca–xZn alloys, Corros. Sci. 64 (2012) 184–197.
[27] H.R. Bakhsheshi-Rad, A. Idris, M.R. Abdul Kadir, S. Farahany, M.Y. Yahya, Characterization and corrosion behavior of biodegradable Mg–Ca and Mg–Ca–Zn implant alloys, Appl. Mech. Mater. 121–126 (2012).
[28] H.R. Bakhsheshi-Rad, M.H. Idris, M.R. Abdul-Kadir, A. Ourdjini, M. Medraj, M. Daroonparvar, et al., Mechanical and bio-corrosion properties of quaternary Mg–Ca–Mn–Zn alloys compared with binary Mg–Ca alloys, Mater. Des. 53 (2014) 283–292.
[29] B. Zhang, Y. Hou, X. Wang, Y. Wang, L. Geng, Mechanical properties, degradation performance and cytotoxicity of Mg–Zn–Ca biomedical alloys with different compositions, Mater. Sci. Eng. C 31 (2011) 1667–1673.
[30] Y. Jang, Z. Tan, C. Jurey, Z. Xu, Z. Dong, B. Collins, et al., Understanding corrosion behavior of Mg–Zn–Ca alloys from subcutaneous mouse model: effect of Zn element concentration and plasma electrolytic oxidation, Mater. Sci. Eng. C 48 (2015) 28–40.
[31] C. Punckt, M. Bolscher, H.H. Rotermund, A.S. Mikhailov, L. Organ, N. Budiansky, et al., Sudden onset of pitting corrosion on stainless steel as a critical phenomenon, Science 305 (2004) 1133–1136.
[32] R.-C. Zeng, J. Zhang, W.-J. Huang, W. Dietzel, K.U. Kainer, C. Blawert, et al., Review of studies on corrosion of magnesium alloys, Trans. Nonferrous Met. Soc. 16 (Supplement 2) (2006) 763–771.
[33] R. Tunold, H. Holtan, M.-B.H. Berge, A. Lasson, R. Steen-Hansen, The corrosion of magnesium in aqueous solution containing chloride ions, Corros. Sci. 17 (1977) 353–365.
[34] G. Song, A. Atrens, M. Dargusch, Influence of microstructure on the corrosion of die cast AZ91D, Corros. Sci. 41 (1998) 249–273.
[35] A. Südholz, Electrochemical properties of intermetallic phases and common impurity elements in magnesium alloys, Electrochem. Solid State Lett. 14 (2011) C5.
[36] P.-R. Cha, H.-S. Han, G.-F. Yang, Y.-C. Kim, K.-H. Hong, S.-C. Lee, et al., Biodegradability engineering of biodegradable Mg alloys: tailoring the electrochemical properties and microstructure of constituent phases, Sci. Rep. 3 (2013).
[37] G. Ben-Hamu, D. Eliezer, K.S. Shin, The role of Si and Ca on new wrought Mg–Zn–Mn based alloy, Mater. Sci. Eng. A 447 (2007) 35–43.